



29 shortening over a 5 km distance at the deposit's toe. The volume of the deformed sediments is  
30 almost the same as the driving debris avalanche deposit. In contrast, the upper, younger  
31 landslide deposit does not show evidence for substrate incorporation or deformation. Instead,  
32 the landslide is a structurally simpler deposit, formed by a debris avalanche that spread freely  
33 along the contemporaneous seafloor (i.e., the top boundary of the intervening sediment unit that  
34 now separates this younger landslide from the older deposit). Our observations show that the  
35 physical characteristics of the substrate on which a landslide is emplaced control the amount of  
36 seafloor incorporation, the potential for secondary seafloor failure, and the total landslide runout  
37 far more than the nature of the original slide material or other characteristics of the source  
38 region. Our results indicate the importance of accounting for substrate interaction when  
39 evaluating submarine landslide deposits, which is often only evident from internal imaging  
40 rather than surface morphological features. If substrate incorporation or deformation is  
41 extensive, then treating landslide deposits as a single entity substantially overestimates the  
42 volume of the initial failure, which is much more important for tsunami generation than  
43 secondary sediment failure.

44 Keywords: flank collapse, Bismarck Sea, landslide, volcano, tsunami, sediment failure

45

## 46 1. Introduction

47 In December 2018, a lateral collapse of the Indonesian volcano Anak Krakatau triggered a  
48 devastating tsunami, killing more than 400 people around the Sunda Strait. The initial collapse  
49 volume calculated at 0.2-0.3 km<sup>3</sup>, is relatively small in the context of volcano sector collapse  
50 (Siebert, 1984; Siebert and Roverato, 2021), but was still capable of generating a highly  
51 destructive tsunami (Gouhier and Paris, 2019; Grilli et al., 2019; Walter et al., 2019). In historic  
52 times, volcanic sector collapses have produced several devastating tsunamis, causing thousands  
53 of casualties around island-arc volcanoes (Auker et al., 2013; Day et al., 2015; Karstens et al.,

54 2019; Watt et al., 2021). The global frequency of historically documented tsunami-generating  
55 events is approximately 50-100 years (Day et al., 2015), including collapses at Oshima-Oshima,  
56 Japan, in 1741, Mt. Unzen, Japan, in 1792, Ritter Island, Papua New Guinea, in 1888, and Anak  
57 Krakatau in 2018 (Walter et al., 2019). This shows that volcanic flank failure and resultant  
58 tsunami genesis poses a serious natural hazard for coastal regions in volcanic settings  
59 worldwide.

60 The Bismarck Archipelago hosts several island-arc volcanoes, of which more than eleven have  
61 recognized offshore debris avalanche deposits (Silver et al., 2009), the product of past lateral  
62 collapses. The most recent and best studied of these is the 1888 Ritter Island collapse (Johnson  
63 et al., 1987; Silver et al., 2009; Ward and Day, 2003; Watt et al., 2019), which is also the largest  
64 volcanic sector collapse globally that has been recorded in historic times (Day et al., 2015).  
65 Recent studies show that the volume of the submarine landslide-derived deposit west of Ritter  
66 is 13 km<sup>3</sup>, but the initial tsunamigenic flank collapse that produced these deposits was only ~2.4  
67 km<sup>3</sup> (Karstens et al., 2019; Watt et al., 2019). This substantial difference in volume between  
68 the offshore deposits and the primary failure illustrates the potential complexity of landslide  
69 processes in volcanic-island settings, where the initial mass movement can lead to extensive  
70 substrate incorporation and secondary failure. Such complexities are not restricted to volcanic  
71 islands, but have also been recognized in submarine landslides in non-volcanic settings (e.g.,  
72 Lenz et al., 2019; Morita et al., 2011; Ogata et al., 2019; Sobiesiak et al., 2018), and constitute  
73 an important general process in the emplacement of subaqueous landslide deposits. Past work  
74 at Ritter, as well as a survey of landslide deposits offshore Montserrat, Lesser Antilles  
75 (Crutchley et al., 2013; Watt et al., 2012a, 2012b), has also shown that both bathymetric and  
76 internal geophysical data (with further insights provided by direct sampling) are required to  
77 accurately reconstruct the complex sequence of transport and dynamics involved in landslide  
78 emplacement offshore volcanic islands. In particular, the internal architecture of deposits is key  
79 to revealing evidence of substrate incorporation, and for the estimation of the initial volume of

80 volcanic debris. The process of substrate incorporation as well as the decoupling of submarine  
81 landslides from the substrate, has also been extensively studied on exhumed ancient mass  
82 transport deposits onshore (Ogata et al., 2019; Sobiesiak et al., 2018). These studies show that  
83 substrate decoupling occurs where a lubricating layer between the landslide and the substrate  
84 prevents the transmission of shear stress from the flow into the substrate (Ogata et al., 2014b;  
85 Sobiesiak et al., 2018) and that substrate incorporation occurs where either the basal drag of the  
86 flow is great enough to plough the slide mass into the substrate, or where a dragged tool (e.g.,  
87 a coherent slide block) is pressed into the substrate's surface at the base of the flow, ripping off  
88 substrate material (Sobiesiak et al., 2018).

89 During a marine geophysical survey on board RV SONNE (SO252), we surveyed the seafloor  
90 around Ritter and the neighboring islands of Sakar and Umboi (Fig. 1). Beside the deposits of  
91 the 1888 Ritter Island sector collapse, we identified two additional, buried landslide deposits  
92 west of Sakar that vary in extent and morphology. These differences relate to distinct patterns  
93 of seafloor interaction and internal structures. Understanding the transport and emplacement  
94 processes that lead to such deposits, and how and why the morphology and extent of deposits  
95 vary, is key to constraining tsunami magnitudes and providing hazard assessments for coastal  
96 regions potentially subject to volcanic-tsunami hazards (Løvholt et al., 2015).

97 The main aim of this paper is to identify the processes that resulted in the two different types  
98 of volcanic landslide deposit observed offshore Sakar, by targeting two objectives. The first  
99 objective is to determine the origin of the seismically imaged deposits. We use high-resolution  
100 2D seismic data to reconstruct the geometry (extent and thickness) of the deposits to test  
101 whether they originated from Umboi, Sakar or Ritter. The second objective is to constrain the  
102 emplacement dynamics of the landslides with a focus on their interaction with the underlying  
103 substrate. We use seismic characteristics such as internal reflection patterns, amplitude  
104 variations, and the configuration of the top and bottom bounding reflectors to interpret the  
105 origin of different sub-facies within the landslide deposits and their relationship to each other,

106 thereby evaluating the extent of the primary failure mass and evidence of substrate  
107 incorporation and deformation.

108

## 109 2. Geological Background

### 110 2.1 Regional tectonics

111 Sakar is a volcanic island located on the southern margin of the Bismarck microplate, forming  
112 a part of the Western Bismarck volcanic arc (Fig. 1). This 1000 km-long volcanic arc extends  
113 onto the larger island of New Britain to the east, and arc volcanism in this setting is associated  
114 with the northward subduction of the Solomon microplate and of a relict slab further west,  
115 where the arc has collided with the New Guinea continental margin (Baldwin et al., 2012;  
116 Honza et al., 1989; Johnson et al., 1987; Taylor, 1979). This tectonically complex zone of  
117 microplates lies in a region of oblique convergence between the Pacific and Australian plates  
118 (Baldwin et al., 2012; Holm and Richards, 2013; Woodhead et al., 2010). The eastern and  
119 western ends of the Bismarck arc are cut by the Bismarck Sea Seismic Lineation, a seismically  
120 active series of left-lateral transform faults and spreading segments separating the South  
121 Bismarck plate and the North Bismarck plate (Baldwin et al., 2012; Taylor, 1979; Fig. 1).

122

### 123 2.2 Geology and Topography

124 Sakar is the northernmost of a group of three islands approximately 25 km west of New Britain,  
125 (Fig. 1). The larger volcanic island of Umboi is 15 km south of Sakar, and the much smaller  
126 island of Ritter – the subaerial remnant of the 1888 lateral collapse – lies in between. Rock  
127 samples show that the volcanism of the western Bismarck arc, including that on Ritter, Umboi  
128 and Sakar, is dominated by basaltic magmas (Johnson, 1977; Woodhead et al., 2010).

129 Sakar has a broadly symmetrical conical form, with gullied slopes that rise steeply to the island  
130 summit. The island diameter at sea level is approximately 8 km, but the entire structure rises  
131 from a base ~1500 m below the sea surface, with a diameter of ~25 km, to a maximum height

132 of ~900 m above sea level. The summit crater is approximately 1.5 km wide and contains a  
133 crater lake (Johnson et al., 1972). The island is formed by this single main volcanic edifice,  
134 which is dominated by porphyritic basaltic lavas, with subsidiary andesites. Around the island  
135 shoreline are volcanoclastic alluvial deposits, and there are parasitic volcanic cones in the  
136 northern part of the island (Johnson et al., 1972). No historical eruptions are known from Sakar,  
137 but several hot springs on the southwestern shore (Johnson et al., 1972), as well as its youthful  
138 morphology, suggest that it is potentially active. Offshore, the island is fringed by coral reefs.  
139 The seafloor offshore Sakar was surveyed in 2004 by the RV Kilo Moana, on a research  
140 expedition that mapped 12 landslide deposits in the Bismarck volcanic arc (Silver et al., 2009).  
141 This expedition investigated in detail the submarine deposits from the lateral collapse of Ritter  
142 in 1888 (Day et al., 2015; Johnson et al., 1987; Karstens et al., 2019; Silver et al., 2009; Ward  
143 and Day, 2003), which travelled between Sakar and Umboi and into the basin northwest of the  
144 islands. It also identified a field of hummocks north of Sakar – a different area from that  
145 described in this paper – and interpreted this to be the blocky facies of a debris avalanche deposit  
146 originating from Sakar. This deposit covers an area of 30 km<sup>2</sup> to a distance of more than 10 km  
147 from the island's coast (Fig. 2). The lack of a collapse scar was explained by later volcanic  
148 growth and the formation of coral reefs within the avalanche's source area. However, several  
149 irregular valleys at the flanks around Sakar indicate potential source areas of landslides (Fig. 2;  
150 Silver et al. 2009).

151

### 152 3. Data and Methods

153 During scientific cruise SO252 on R/V SONNE in November/December 2016, we collected 2D  
154 multichannel seismic data using a 250 m-long (160 channels) streamer system with a group  
155 spacing of 1.56 m [dataset](Berndt et al., 2021b). As the seismic source, we used two GI  
156 airguns, shot in harmonic mode (105/105 cubic inch). In total, we collected 680 km of seismic

157 reflection profiles (Fig. 1). The data were processed with a 10, 45, 250, 400 Hz bandpass filter,  
158 a normal moveout correction (constant velocity: 1495 m/s, derived from CTD measurements),  
159 and a post-stack 2D-stolt-migration using a constant velocity of 1500 m/s. The bathymetry of  
160 the survey area was mapped using two multibeam systems (Kongsberg EM710 and EM122)  
161 with a horizontal resolution of 25 m [dataset](Berndt et al., 2021a). For the maps shown in this  
162 study, we merged the acquired high-resolution bathymetry grid with a low-resolution global  
163 GEBCO grid. Detailed acquisition and processing descriptions can be found in the SO252  
164 cruise report (Berndt et al., 2016).

165 The range of data collected on cruise SO252 also includes a 3D seismic dataset (Karstens et al.,  
166 2019), high-resolution sub-bottom echosounder profiles (Parasound P70 system) and high-  
167 resolution video sledge derived photography (Watt et al., 2019), as well as grab samples. To  
168 derive a 2D velocity model by forward modeling, six three-component ocean bottom  
169 seismometers (OBS) were deployed along a profile within the 3D seismic cube.

170 Depth, thickness, and volume calculations of sedimentary units mapped using the 2D seismic  
171 data were carried out with a seismic velocity of 1760 m/s, derived from OBS experiments  
172 (Karstens et al., 2019). Areas and volumes were determined by picking the top and base  
173 reflections of sedimentary units on cross-cutting seismic profiles. Relative shortening in units  
174 with resolvable compressional structures along the profiles was graphically estimated, using  
175 the ratio between the observed extent of the compressional zone and the length of mappable  
176 reflections within the seismic data along the deformed reflectors at zero vertical exaggeration.  
177 As parts of the compressional structures cannot be resolved properly in the seismic data,  
178 shortening values have to be considered minimum estimates. Absolute displacement values of  
179 thrust faults were calculated by dividing the picked horizontal distance of a thrust horizon  
180 overlying its undeformed counterpart by the cosine of the fault dip angle.

181

182 4. Results

183 4.1 Seismic facies

184 The stratigraphy northwest of Sakar and Ritter, and north of Umboi, was extensively imaged  
185 within the seismic data collected during cruise SO252, with examples shown in Figs. 3 and 4.  
186 The data reveal two generally different seismic facies: one defined by continuous and parallel  
187 reflections and a second one characterized by chaotic and rather transparent (i.e., lower  
188 amplitude) seismic reflections.

189 The dominant sub-seafloor facies consists of continuous and parallel reflections. This facies is  
190 typified by laterally coherent reflections with generally consistent amplitudes. The reflections  
191 appear relatively homogenous and are sub-horizontal, lacking any hummocky or steeply  
192 dipping morphological features, and representing the seismic image of well-bedded sediments.  
193 Subsequently we will refer to this facies as the well-bedded sediment facies.

194 The second facies, characterized by chaotic and relatively transparent reflections, occurs in two  
195 discrete and broadly horizontal packages, that interrupt the well-bedded sediment facies  
196 northwest of Sakar. We divide this chaotic facies into two types. The first type contains irregular  
197 surfaces with dipping, sometimes irregular or wavy top boundary reflections. This sub-facies  
198 has top and bottom boundaries with high seismic amplitudes, while it is internally chaotic, with  
199 most parts being significantly more transparent than the well-bedded sediment facies. This  
200 internally chaotic sub-facies is present in two distinct packages of reflections on and near the  
201 western flank of Sakar. We consider these packages to represent landslide deposits: a shallow  
202 deposit subsequently referred to as Sakar Landslide Deposit 1 (SLD1) and a deeper deposit  
203 referred to as Sakar Landslide Deposit 2 (SLD2), which we describe in detail within the  
204 following subsections. The second chaotic sub-facies is relatively transparent, too, but contains  
205 internal reflections that are parallel-bedded and mostly continuous. This sub-facies occurs as a  
206 distal continuation of the internally chaotic sub-facies in SLD2. We interpret its characteristics



207 as corresponding to deformed bedded sediments, forming the outer part of SLD2, and will  
208 subsequently refer to this as the deformed sediment sub-facies.

209

#### 210 4.2 Seafloor morphology

211 The submarine morphology northwest of Sakar is dominated by a sub-circular field of 107  
212 randomly distributed hummocks (i.e., positive, relatively steep-sided bathymetric features  
213 encircled by a clear break in slope), covering an area of 240 km<sup>2</sup> with long-axis diameters >100  
214 m (Fig. 2). This hummock field is separated from that previously identified north of Sakar by  
215 Silver et al. (2009), and partially overlaps with the distal part of the transport path of the 1888  
216 Ritter Island landslide deposits (Fig. 2; Day et al., 2015; Watt et al., 2019). Within the hummock  
217 field northwest of Sakar, 92 hummocks have maximum diameters between 100 and 500 m (at  
218 the basal break in slope), 23 between 500 and 1,000 m and two between 1,000 and 1,100 m,  
219 covering individual surface areas between ~0.05 km<sup>2</sup> and ~1.21 km<sup>2</sup>. The second largest  
220 hummock was transected by two seismic profiles (Fig. 3A, C), and covers a surface area of ~1  
221 km<sup>2</sup> with a height > 80 m above the surrounding seafloor. The flanks of this hummock continue  
222 down to 120 m below the seafloor and are resolvable to the center of SLD2 (internally chaotic  
223 sub-facies) (Fig. 3). In contrast, the basal reflection of SLD1 continues below most of the other,  
224 smaller hummocks that are transected by seismic profiles, but is bent upwards, which we  
225 attribute to seismic velocity pull-up. Most of the hummocks observable at the present-day  
226 seafloor therefore appear to be rooted within SLD1 (Fig. 3B), and are partially buried by  
227 overlying sediment. Some hummocks show an internal seismic stratification that is not parallel  
228 to the surrounding stratigraphy (Figs. 3B, C), while some show chaotic internal reflections (Fig.  
229 3C) and others show no visible internal reflections (Fig. 3B), which is most likely a problem of  
230 seismic imaging. None of these hummocks has a conical shape, comparable to the conic  
231 landforms northwest of Ritter and south of Sakar (Karstens et al., 2019); instead, they appear

232 elongated and sub-angular, but without a preferred orientation. Their broad form is similar to  
233 volcanic landslide blocks in other offshore settings, such as those offshore Montserrat (Watt et  
234 al., 2012b) or El Hierro, Canary Islands (Masson et al., 2002), or in many subaerial volcanic  
235 settings (e.g., Yoshida et al., 2012). The average slope between the hummocks dips  $2.5^\circ$   
236 seaward close to Sakar and  $< 0.5^\circ$  at the north-western limits of the hummock field. Outside of  
237 the hummocky field the seafloor is generally smooth and flat (Fig. 2) with an overall slope  
238 gradient below  $0.5^\circ$ . However, there are areas within the field containing parallel ridges  
239 trending southeast-northwest (Fig. 2) with wavelengths of  $\sim 200$  m and amplitudes of  $\sim 5$  m;  
240 and a relatively small field of elongated seafloor depressions with diameters between 200 and  
241 500 m and 5 to 15 m depth. Northwest of the hummock field the seafloor morphology is  
242 dominated by several smooth-surfaced lobes, interpreted as the distal deposits of the 1888 Ritter  
243 Island collapse (Watt et al., 2019).

244 Our bathymetric data show that the field of hummocks north of Sakar (cf. Silver et al., 2009)  
245 has block sizes and distribution similar to those in the north-western field mapped here. As  
246 there are no seismic data imaging the subsurface of the second hummock field to the north, and  
247 because it is separated from the one mapped here by several kilometers, we do not further  
248 investigate the area north of Sakar within this paper.

249

## 250 4.3 Landslide deposit stratigraphy

### 251 4.3.1 Sakar Landslide Deposit 1 stratigraphy

252 Directly below the seafloor reflection west of Sakar, a  $\sim 10$  m-thick unit with chaotic internal  
253 reflections is located (Fig. 3A, 4). Watt et al. (2019) interpreted it to be the deposit of the 1888  
254 Ritter Island sector collapse. The Ritter deposit overlies a  $\sim 50$  m-thick package of well-stratified  
255 reflections (Fig. 4), but to the east, closer towards the slope of Sakar, it overlies SLD1. In 2D  
256 profiles, the latter forms a tapering, wedge-shaped deposit, seismically characterized by the  
257 internally chaotic sub-facies, with an average thickness of 67 m (Figs. 3, 4). SLD1 can be

258 correlated across multiple profiles, defining a laterally fan-shaped deposit (Fig. 1) extending  
259 over an area of ~250 km<sup>2</sup> with a volume of ~15.5 km<sup>3</sup>. Close to the flank of Sakar, the boundary  
260 between SLD1 and the underlying bedded stratigraphy, which has an increasingly chaotic  
261 general appearance in seismic reflection profiles, becomes obscure (Fig. 4A). Although the  
262 general seismic appearance of SLD1 corresponds to the internally chaotic sub-facies, at least  
263 two continuous internal reflections can be traced over a distance of 1 km, with a seismic  
264 waveform that consists of one peak overlying one trough.

265 SLD1 is thickest on the slope of Sakar (slope gradient 2.5 °), tapering to the west. In this area,  
266 its top boundary reflection is indistinguishable from the seafloor reflection, which has a  
267 hummocky seismic appearance. The lateral margins of SLD1 as well as the area where its upper  
268 surface is indistinguishable from the seafloor (on the outer flank of Sakar), correlate with the  
269 margins of the hummock field northwest of Sakar observed in the bathymetry (Fig. 2). The  
270 volume stated above includes the hummocks intersected by the seismic data that appear to be  
271 rooted within SLD1; hummocks between and off the seismic profiles, as well as the large block  
272 shown in Fig. 3A, which appears to be rooted within SLD2, are not included. Due to the limited  
273 coverage of the 2D seismic lines, the extent of SLD1 could not be mapped entirely. Extent and  
274 volume thus have to be considered minimum values.

275

#### 276 4.3.2. Sakar Landslide Deposit 2 stratigraphy

277 At a depth of 60 – 70 m below the seafloor, the top boundary of SLD2 extends over an area of  
278 590 km<sup>2</sup> (Fig. 1) and has an elongated shape. The average thickness of the deposit is 71 m,  
279 which remains relatively consistent over the entire extent. Deposit thickness tapers to less than  
280 60 m at the north-eastern and south-western margins. We divide the deposit into three parts: A  
281 proximal part close to Sakar, seismically characterized by the internally chaotic sub-facies  
282 (similar to SLD1); a middle part, characterized by the deformed sediment sub-facies; and a  
283 distal toe consisting of the deformed sediment sub-facies as well, but with more coherent

284 reflections that show extensively folded and thrust-faulted reflections (Fig. 4B). All three parts  
285 are included in the volume and extent values stated here.

286 In the southeasternmost part of the seismic profile in Fig. 4, the proximal part of SLD2 is  
287 separated from SLD1 by a continuous reflection package of ~15 m maximum thickness over a  
288 downslope distance of ~3 km. Close to the outer flank of Sakar, seismic reflections are generally  
289 chaotic, and amplitudes decrease with time in respect to depth more strongly than in the basin  
290 west of the island. Because of this, it is very difficult to distinguish the bottom boundary of the  
291 internally chaotic sub-facies in SLD2. For this study, we chose the first continuous high-  
292 amplitude reflection to define the base of SLD2 in this area, but the true boundary may be  
293 located even deeper. Therefore, we consider the volume of this part of SLD2, of 12.5 km<sup>3</sup>, as a  
294 minimum volume. The depth of the continuous basal reflection varies within +/- 10 m, resulting  
295 in a proximal deposit thickness of 47 m to 61 m (Fig. 4). Within the seismic data the surface of  
296 the proximal SLD2 has an apparent downslope angle between 0.5 and 2.0 °, following the  
297 general slope trend close to Sakar.

298 The downslope limit of the proximal part of SLD2 coincides with the appearance of more  
299 continuous internal reflections (the transition from the internally chaotic to the deformed  
300 sediment sub-facies), a basal upward step of the deposit's bottom boundary reflection, and a  
301 break in the slope gradient. This defines the start of the middle part of SLD2. Internally, the  
302 reflections in this part of SLD2 have lower amplitudes than the bounding stratigraphy but show  
303 visible continuity over ~ 17 km distance. This continuity is only disrupted by vertical seismic  
304 anomalies of upward bent reflections (Fig. 4B). Across the transition from the proximal to the  
305 middle part of SLD2, the top reflections are undulated, over a distance of more than 5 km (Fig.  
306 4B). This upper surface morphology consists of seven undulations with wavelengths between  
307 500 m and 1300 m and amplitudes between 3 m and > 8 m. These transition, to the northwest  
308 into reflections concordant to the well-bedded sediment facies above (Fig. 4B). Directly below  
309 the top reflection, a ~10 m thick package of continuous reflections with higher coherency than

310 the internal reflections below is resolvable, until it is cut by the deformation marking the start  
311 of the distal toe of the deposit (Fig. 4B). The upper surface of SLD2 transitions from a  
312 (apparent) north-western dip of  $0.16^\circ$  to an (apparent) south-eastern dip of  $0.17^\circ$  towards the  
313 deposit's toe. The bottom boundary reflection steps upwards from the proximal part of SLD2,  
314 becoming shallower by  $\sim 23$  m over a downslope distance of  $\sim 1000$  m. This marks the bottom  
315 boundary-limit between the internally chaotic sub-facies in the proximal part and the deformed  
316 sediment sub-facies in the middle part of SLD2. Beyond this step, the basal reflection is  
317 generally continuous and concordant with the underlying stratigraphy, and its amplitude  
318 decreases towards the distal part of SLD2.

319 The distal part of SLD2 is dominated by thrusting and folding. The boundary between the  
320 middle and distal part is characterized by the appearance of higher-amplitude internal  
321 reflections, in which compressional structures become clearly visible. At least five thrust faults  
322 can be identified over a downslope distance of more than 5 km, with fault dip angles between  
323  $12^\circ$  and  $17^\circ$  and an apparent southeast dip direction, parallel to the profile direction (Fig. 5C).  
324 Between the thrusts and folds, the seismic reflections are irregularly deformed, with a chaotic  
325 appearance and without resolvable faulting or folding. Due to this chaotic nature, absolute  
326 displacement calculations were only possible for two of the thrust faults, giving individual  
327 displacement values of 73 m and 82 m ( $\pm 20$  m picking uncertainty due to the chaotic seismic  
328 character). From relative graphical estimations (see 3. Data and Methods) a horizontal  
329 shortening of 27% caused by thrusting and folding is estimated over the most distal 5 km of the  
330 toe region (in the direction of the seismic profile; Fig. 5C).

331 The deformation of both the middle and distal part of SLD2 occurs on the same basal reflection  
332 and suggests that this represents the primary shear surface. The reflections directly below this  
333 basal shear surface are coherent, but within the first 25 ms-interval they are more transparent  
334 than deeper reflections, with evidence for some disturbance (Fig. 4B), suggesting a narrow zone  
335 of additional shear, decreasing downwards, and terminating at the base of this 25 ms interval.

336 Below the distal toe region, reflections are truncated by a series of apparently northeast and  
337 southeast dipping normal faults (Fig. 4B). The middle and distal part of SLD2, all comprising  
338 the deformed sediment sub-facies, have a volume of  $\sim 13.5 \text{ km}^3$ .

339

## 340 5. Discussion

### 341 5.1 Origin and emplacement of SLD1

342 SLD1 is characterized by a fan-shaped hummocky topography and its seismic character  
343 corresponds to the internally chaotic sub-facies. Hummocky topographies around many  
344 volcanoes globally are representative of the blocky facies of debris avalanche deposits (e.g.  
345 Mount St Helens, Glicken 1996), although broadly comparable topographies may also be  
346 formed by scattered volcanic vents and cones (e.g. Azores, Weiß et al. 2015), or by erosional  
347 processes (e.g. Ritter Island, Karstens et al. 2019). Internal reflections indicate stratification  
348 within the hummocks of SLD1, and these can be used as an indicator of their origin. Reflections  
349 parallel to the underlying stratigraphy would be expected if the hummocks are the result of  
350 erosion, while conical forms, with reflections parallel to the flanks of the hummock or with  
351 broken, upward-bended reflections at the base of the hummock, would be typical for volcanic  
352 cones (both examples can be found west of Ritter; Karstens et al., 2019). However, most of the  
353 hummocks off Sakar lack internal stratification or have internal reflections with a dip that is  
354 discordant with that of the surrounding stratigraphy. They also have irregular, sub-angular  
355 shapes, steep sides and in some cases relatively flat tops. Together, these observations suggest  
356 that the hummocks represent transported blocks. Due to the fan-shaped distribution of these  
357 blocks at the foot of Sakar we interpret them as being from a common source and emplaced in  
358 a single mass movement, and that they thus represent the blocky facies of a debris avalanche  
359 deposit. The random distribution of these blocks within the fan is indicative of a freely  
360 spreading avalanche (Yoshida et al., 2012). This implies that the flow velocity in the

361 emplacement direction was not significantly higher than the flow-perpendicular spreading  
362 velocity (Crutchley et al., 2013).

363 The areal extent of the northwestern block field in the bathymetric data matches the seismic  
364 extent of SLD1, except in the northwesternmost part of the profiles, where the burial depth of  
365 SLD1 is too deep for blocks to protrude at the seafloor. This indicates that the bathymetric  
366 expression can be used to constrain the minimum extent of the blocky part of the debris  
367 avalanche but does not resolve the margins of the shallowly buried deposit. The high seismic  
368 amplitude of the boundary reflections is indicative of a significant change in seismic impedance,  
369 implying a different nature of the deposited material within and around SLD1. Seismic  
370 reflections within SLD1 are generally discontinuous, chaotic, and transparent. However, there  
371 are some coherent reflections extending laterally up to 1000 m. These suggest that the deposit  
372 was not emplaced as a simple, fully disaggregated one-directional flow or avalanche. The  
373 reflections may either indicate deposition in separate stages or phases of one major event,  
374 representing the interface between different flow lobes or pulses (e.g., Deposit 1, Montserrat,  
375 Crutchley et al., 2013; Lebas et al., 2011), or they may correspond to a thin (i.e., sub-seismic)  
376 unit of hemi-pelagic sediments indicating a period of normal sedimentation between unrelated  
377 flank collapse events. As these reflections are not visible on all seismic lines that image the  
378 deposit and are laterally restricted, we consider the first scenario more likely.

379 Due to the geometry and location of SLD1, the debris avalanche most likely originated from  
380 Sakar. There are multiple morphological structures that may reflect the scars of past sector  
381 collapses onshore Sakar Island (Silver et al., 2009). However, none of them correlates spatially  
382 with the deposit, and it is ambiguous if they have large enough dimensions to be the source of  
383 a  $>10 \text{ km}^3$  landslide deposit, suggesting that younger volcanic activity has entirely overprinted  
384 the onshore part of the SLD1 collapse scarp.

385 The hummocky proximal morphology of SLD1, in combination with its fan-shaped extent and  
386 chaotic internal structure, unequivocally shows that it is a submarine landslide deposit (Frey-

387 Martínez et al., 2006). Similar deposits with volcanic origin have been identified in many  
388 locations (Watt et al., 2021) including Montserrat (Deposit 1; Watt et al. 2012b, a; Crutchley et  
389 al. 2013; Karstens et al. 2013) and Fogo, Cape Verde (Day et al., 1999; Le Bas et al., 2007;  
390 Masson et al., 2008). The fan shape of the deposit suggests a cohesionless flow dominated by  
391 energy dissipation through granular particle interactions, which is typical for freely-spreading  
392 heterogenous and generally coarse-grained volcanic debris avalanches (Mulder and Cochonat,  
393 1996; Watt et al., 2012a, Watt et al., 2021).

394 Within SLD1, there is no seismic or bathymetric evidence for the secondary incorporation of  
395 underlying material (including that of SLD2). According to Sobiesiak et al. (2018), a  
396 decoupling of the sliding mass from the substrate, “free-slip flow”, occurs where shear stress  
397 transmission from the flow into the substrate is prevented by a lubricating layer. The study  
398 suggests the formation of this lubricating layer by one (or a combination) of the following  
399 mechanisms: hydroplaning, shear wetting, and/or liquefaction. During hydroplaning the  
400 hydrodynamic water pressure at the flow front increases and is transferred into the underlying  
401 bed, forming a water-rich sediment layer between flow and substrate (Mohrig et al., 1998).  
402 Shear wetting describes the generation of a soft, diluted, lubricating layer due to high shear  
403 rates between the water and the sediment boundary during flow (De Blasio et al., 2005). Ogata  
404 et al. (2014a) describe liquefaction of poorly consolidated sands where the induced shear of the  
405 flow causes a loss of grain contacts within the sand layers. As the flow stops, these liquified  
406 sands inject upwards into the basal flow deposit. Our seismic data do not provide the resolution  
407 to allow us to distinguish between these different processes (such as the observation of basal  
408 injections of sand (e.g. vertical fluid escape structures), which would be indicative for  
409 liquefaction (Ogata et al., 2014a, 2012), and while we cannot provide further constraints, we  
410 consider it likely that one or a combination of these processes led to a decoupling of the SLD1  
411 debris avalanche and the contemporaneous seafloor.



412 Southwest-northeast trending ridges within the hummock field and north of Sakar (Fig. 2) are  
413 most likely related to later sedimentary processes, e.g., sediment waves (Pope et al., 2018).  
414 They also could be related to the deposition of the 1888 Ritter Island collapse debris flow (Watt  
415 et al. 2019), but in either case, we do not interpret them as being directly associated with SLD1.  
416 As the Ritter Island 1888 deposits partially overlap with the SLD1 hummock field (Fig. 2), we  
417 cannot exclude some erosion of SLD1 by the Ritter Island debris flow, although the burial depth  
418 of SLD1 in most places is deeper than the bottom boundary of the Ritter Island, and any erosion  
419 is thus not likely to have had a major impact on the morphology or our estimated volume of  
420 SLD1.

421

## 422 5.2 Origin and emplacement of SLD2

423 SLD2 extends from the outer flank of Sakar 30 km into the neighboring basin northwest of  
424 Sakar and Umboi (Fig. 1). Based on its location and its shape, an origin from Umboi, Sakar or  
425 Ritter may be possible. However, an origin from the relatively small edifice of Ritter is unlikely  
426 due to the large volume of the proximal component (12.5 km<sup>3</sup>) and because the deposit lies  
427 partly on the flanks of Sakar, which would require an element of upslope, northward bending  
428 transport and deposition. The shape and thinning pattern are most consistent with a landslide  
429 originating from the western slope of Sakar. This agrees with the direction of deformation  
430 patterns in the outer parts of SLD2, indicating northwestward compressional deformation in the  
431 toe domain (Fig. 5).

432 The proximal part of SLD2 is seismically characterized by the internally chaotic sub-facies  
433 (Fig. 4). This is similar to the overall seismic image of SLD1, suggesting that this part of the  
434 deposit originated as a volcanic debris avalanche, similar to SLD1. The apparent rooting of a  
435 large, transported block that protrudes from SLD2 to the seafloor (Fig. 3A, C) supports this  
436 interpretation, and it is likely that the surface of SLD2 contained many such blocks or  
437 hummocks, the majority of which are now buried and no longer evident at the seafloor. The

438 outer margin of the internally chaotic sub-facies shows a direct lateral transition into the  
439 deformed sediment sub-facies (Fig. 4B). Hence, SLD2 shows characteristics typical for  
440 volcanic debris avalanches off volcanic islands, but at the same time its middle and distal part  
441 comprise large volume of deformed pre-existing sediments, and SLD2 thus represents a  
442 composite deposit of volcanic material and seafloor sediments.

443 As described above, the middle part of SLD2 contains a discrete unit in its uppermost part (Fig.  
444 4B), which may indicate the deposit of an overrunning flow. This unit has an undulated upper  
445 surface, and although this morphology could be a result of later sedimentary processes, its  
446 seismic image is markedly different from bedforms typically associated with sediment waves,  
447 (Pope et al., 2018), and we interpret this undulating form to be a primary characteristic of the  
448 upper surface of SLD2.

449 The transition from a proximal debris avalanche deposit to deformed seafloor sediments  
450 (marked by basal step, Fig. 4B) suggests that SLD2 originated as a debris avalanche from Sakar  
451 that incised into the substrate, as shown by the lateral transition between the internally chaotic  
452 sub-facies and the deformed sediment beyond. This transition indicates that some seafloor  
453 sediment must be incorporated within the proximal, internally chaotic part of SLD2, unless this  
454 pre-existing sediment was entirely evacuated from this area. Beyond the proximal part of SLD2,  
455 some evacuated sediment, or a more mobile part of the driving debris avalanche, may have  
456 overran the pre-existing seafloor, giving rise to the discrete uppermost unit in the middle part  
457 of SLD2. This overrunning flow may have facilitated the downslope-propagating deformation  
458 of the underlying seafloor sediment (i.e., the deformed sediment sub-facies of SLD2), which  
459 formed beyond the front of the driving debris avalanche (e.g., see processes discussed in Watt  
460 et al., 2012b) (Fig. 6). This seafloor sediment package shows strong evidence of in-situ  
461 compressional deformation, particularly at its toe, but was not evacuated, defining a frontally  
462 confined mass transport deposit (Frey-Martínez et al., 2006). Beyond the limits of the frontally  
463 confined margin (Fig. 4B), we cannot find seismic indications for further mass transport,

464 although it is possible that the thin, distal parts of an overrunning flow are not resolvable within  
465 our seismic data.

466 The seismic analyses of debris avalanche deposits offshore Montserrat revealed composite  
467 deposits consisting of a volcanic subunit and a subunit of deformed and mobilized seafloor  
468 sediments (Deposits 2 and 8, Watt et al. 2012b, a; Crutchley et al. 2013), similar to SLD2. These  
469 composite deposits formed as the result of the collision of a volcanic debris avalanche with  
470 seafloor sediments, resulting in their mobilization and deformation. This interpretation was  
471 confirmed by IODP expedition 340 (Le Friant, 2015), which revealed the absence of volcanic  
472 debris avalanche deposits within the seismically transparent, distal subunit of Montserrat  
473 Deposit 2 and of comparable deposits offshore Martinique. The processes involved in the  
474 interaction between volcanic debris avalanches and underlying seafloor sediments are complex  
475 and there are various potential mobilization mechanisms (Watt et al. 2012b; Le Friant 2015).

476 Studies on exhumed ancient mass transport deposits onshore confirm the potential composite  
477 nature of landslide deposits. “Megabreccia” deposits in the Paleogene Friuli Basin  
478 (Italy/Slovenia) were interpreted as the result of bipartite slide masses with a lower cohesive  
479 blocky flow and an upper turbulent flow, deeply eroding into and deforming the substrate  
480 (Ogata et al., 2014b). Sobiesiak et al. (2018) discuss substrate incorporation mechanisms such  
481 as that driven by a basal drag of the flow mass great enough for it to erode into the substrate,  
482 ripping off the latter and incorporating it into the flow. Alternatively, similar effects may occur  
483 by the dragging of a tool (e.g., a transported block) pressed against the substrate and ripping it  
484 off, or by peel-back, where the substrate is pushed along a basal weak layer laterally bounded  
485 by sub-vertical shear zones. Ogata et al. (2019) suggest similar substrate incorporation  
486 processes such as the erosion of positive paleobathymetric highs, and the transfer of inertial  
487 stress of a moving flow into the substrate due to an abrupt change of the slope angle, where the  
488 momentum of well-lithified blocks is transferred into the substrate as the slide comes to rest.

489 Large blocks such as that imaged in Fig. 3A could potentially have functioned as tools, eroding  
490 the slide mass into the substrate where the gradient of Sakar's slope decreases. However, due  
491 to the limited resolution of our seismic data we cannot identify if one of the specific mechanisms  
492 outlined above represented the dominant mode of substrate erosion by the SLD2 debris  
493 avalanche.

494 The deformation pattern in the outer region of SLD2 is typical for the deposits of frontally  
495 confined landslides (Frey-Martínez et al., 2006) and has been observed in non-volcanic  
496 submarine mass-movements (e.g., Oregon, USA, Lenz et al., 2019; Shimokita peninsula,  
497 northeast Japan, Morita et al., 2011) as well as volcanic settings (e.g., Deposit 8 offshore  
498 Montserrat, Watt et al., 2012b). Substrate deformation as the result of the emplacement of  
499 volcanic debris avalanches has been seismically documented offshore Montserrat (Crutchley et  
500 al., 2013; Watt et al., 2012b, 2012a) and at Ritter Island (Karstens et al., 2019; Watt et al.,  
501 2019), where deformed and incorporated sediments contribute 80% of the total slide volume.  
502 Potential factors that define the absolute limit of deformation at the toe of SLD2 could be the  
503 reversal of the slope direction, adding gravitational forces to the shear resistance of the  
504 sediments against progressive shear failure of the deforming sediments as well as a topographic  
505 effect caused by several normal faults cutting through the strata below (Fig. 4B).

506 For the deformation of the well-bedded sediment sub-facies of SLD2, we favor a combined  
507 substrate deformation model, as follow (Fig. 6): Substrate incorporation (i.e., physical mixing  
508 of the volcanic debris avalanche with seafloor sediments) did not reach beyond the basal step  
509 that marks the foot of the internally chaotic sub-facies of SLD2. This coincides with a break in  
510 the slope gradient, (Fig. 4). The initial loading that triggered frontal deformation beyond this  
511 point could have been the result of a transfer of the blocky debris avalanche's momentum as it  
512 decelerated into the substrate, progressively increasing the shear stress on the sediment, causing  
513 disaggregation, deformation, and compression. Added to this, an overrunning flow may have  
514 facilitated propagation of deformation in the underlying sediment, but the potential mechanisms

515 of this process remain ambiguous. An overrunning flow could potentially liquify underlying  
516 sediments by increasing the pore pressure due to grain reorganization during shearing  
517 (Hornbach et al., 2015; Ogata et al., 2014a) similar to the shear failure of sensitive clay deposits  
518 onshore (Bjerrum, 1955; Quinn et al., 2012). With the vertical seismic anomalies in the middle  
519 SLD2 (Fig. 4B), we find indications for fluid migration pathways (Gee et al., 2007) which could  
520 represent liquefaction. However, we cannot rule out that these structures represent seismic  
521 imaging artifacts. A mechanism of shear coupling, as proposed for paleo-landslide deposits in  
522 the Karoo Basin, South Africa (Van Der Merwe et al., 2011) and discussed for Deposit 8 off  
523 Montserrat (Watt et al., 2012b), where the motion of an overrunning flow exerts forces on the  
524 underlying strata leading to deformation, appears less plausible for SLD2. Seismic evidence for  
525 an overrunning flow is only visible in the middle part of SLD2, whereas if this flow was the  
526 main agent of deformation via shear coupling, we would expect it to be present over the entire  
527 deposit, an alternative model that could explain the seafloor sediment beyond the margin of  
528 SLD2 could be that the younger emplacement of SLD1 loaded the older deposits, and triggered  
529 failure downslope of these via the shear failure mechanisms described above. Similar secondary  
530 seafloor mobilization and deformation of deeper sediment packages, including thrust faulting  
531 and folding, has been observed for non-volcanic landslides, e.g. offshore Oregon, where a series  
532 of slide blocks have caused deformation and horizontal compaction of underlying sediments  
533 within a 10 km area (Lenz et al., 2019). However, because the sediment failure in SLD2 is  
534 confined to a package that coincides with both the upper and lower boundaries of its proximal  
535 part, and does not affect younger sediment, a role for SLD1 in this process would only make  
536 sense if there was no time gap between SLD1 and SLD2. This is not the case, because we  
537 observe a package of sediment, partly onlapping on the top boundary of SLD2, that separates  
538 the two landslides (Fig. 4B).

539 A further possible model is that both SLD1 and SLD2 are part of one multistage sector collapse,  
540 whereby the deeper unit slowly crept downslope (forming SLD2), until the slope stability

541 reached a critical point and the shallower flank failed, resulting in a collapse that emplaced  
542 SLD1. This type of process was postulated by Karstens *et al.* 2019 for the 1888 sector collapse  
543 of Ritter Island. Such slow, deep-seated deformations are known from other volcanoes, e.g. Mt.  
544 Etna, Sicily (Urlaub *et al.*, 2018). Again, the similar proximal characteristics of SLD1 and  
545 SLD2, and the observation of reflections separating the two deposits, indicates a time gap  
546 between them that implies they are entirely separate lateral collapses. This does not preclude  
547 that the emplacement of both debris avalanches could have been preceded by prolonged gradual  
548 deformation at the base of Sakar's flanks that promoted instability, comparable to processes at  
549 Ritter Island (Karstens *et al.*, 2019) and around other volcanoes.

550 The base of SLD2 is defined by a mostly continuous, high-amplitude reflection representing a  
551 basal shear surface for the deformation of the sediment package above. However, below this  
552 reflection, the well-stratified sediments appear more transparent than further below (Fig. 4). A  
553 second strong reflection about 25 ms TWT below may represent another, secondary basal shear  
554 surface. This second reflection correlates vertically with the depth of the proximal chaotic part  
555 of the unit. As the reflections between both surfaces are weak and transparent, but not deformed,  
556 this may represent a zone of deeper, distributed deformation, less extensive than that within  
557 SLD2 above. The development of a basal shear zone, with different layers of shearing, rather  
558 than one single basal shear surface has been described on onshore exhumed mass transport  
559 deposits (Ogata *et al.*, 2014a; Sobiesiak *et al.*, 2018). The seismic data are inconclusive in  
560 indicating if this basal shear zone involved shear of the sedimentary strata, or just mobilization  
561 of pore fluids.

562

### 563 5.3 Dissimilarity of two landslide deposits from Sakar

564 The results described here show that Sakar has produced at least two voluminous debris  
565 avalanches, deposited on the western submerged island slope and the basin floor to the  
566 northwest. Because both debris avalanches are the result of sector collapse (i.e., they have

567 mobilized large parts of the flank of the same island) it may be expected that they have a similar  
568 composition and that their dynamic evolution was similar. However, while SLD1 appears to  
569 consist completely of volcanic debris avalanche material, only the proximal part of SLD2 hosts  
570 a debris avalanche component. The middle and distal parts of the deposit consist of deformed  
571 seafloor sediments. The volumes of SLD1 and the proximal, internally chaotic sub-facies of  
572 SLD2 are nearly equal. However, the entire SLD2, when including the deformed-sediment  
573 facies, has twice the volume of SLD1. The fan-shape of SLD1, indicating free-spreading of a  
574 cohesionless flow, contrasts with the elongated shape of SLD2, indicating a concentration of  
575 forces in one primary direction, equivalent to the direction of mass movement during the initial  
576 stage of a debris avalanche. The proximal part of SLD2 most likely eroded into and partly  
577 overran the substrate (coupling of flow and substrate), causing deformation in the frontal  
578 direction, while the seismically imageable part of SLD1 spread along and above the pre-existing  
579 seafloor (decoupling of flow and substrate).

580 Seismic interpretations of marine landslide deposits off volcanic islands in the Lesser Antilles  
581 have shown that debris avalanches can incorporate large volumes of substrate during transport  
582 (Deplus et al., 2001; Le Friant et al., 2003; Watt et al., 2012b, 2012a). In a most basic sense,  
583 the process of substrate incorporation into moving debris is an energy exchange between the  
584 flowing debris mass and the initially static seafloor sediments, where kinetic energy of the  
585 flowing mass is consumed to put the static mass in motion. The required amount of energy  
586 depends on the stability of the seafloor sediments, which is controlled by the slope gradient and  
587 the thickness of the sediment layer (Mangeney et al., 2010), but also by the type of the substrate  
588 material and its shear strength. The two deposits examined in this study differ in the nature of  
589 their substrate: the continuation of the sedimentary well-bedded seismic facies underneath the  
590 proximal part of SLD2 (albeit poorly imaged) suggests that it was deposited on relatively fine-  
591 grained and water-saturated seafloor sediment (i.e., typical basin-infilling sediment), that  
592 typically has a low shear resistance. This would have promoted incorporation and a proximal

593 incision of the debris avalanche mass into the substrata. In contrast, the base of SLD1 coincides  
594 with a package of chaotic reflections on the flanks of Sakar, separating it from the proximal  
595 part of SLD2, and in some profiles corresponds directly with the upper part of SLD2. We  
596 interpret this substrate as likely comprising coarse-grained, heterogenous volcanic material  
597 derived from the flanks of Sakar, which would be much harder to mobilize than the hemipelagic  
598 seafloor sediments of the basin floor (Karstens et al., 2013) – the sediment type on which SLD2  
599 was emplaced. Because of this, SLD1 slid decoupled from its base. Landslide deposits are  
600 considered to generally have a higher resistance to being eroded and incorporated into  
601 overflowing landslide masses (Alves and Lourenço, 2010). Outcrop-oriented studies on  
602 sedimentary mélanges link different mechanisms of substrate incorporation not only to the  
603 physiographic setting, but also to different lithological characteristics of the associated mass  
604 transport deposits (Ogata et al., 2019). Combined with our interpretations of SLD1 and SLD2,  
605 this suggests that the substrate is a major control on the incorporation of seafloor sediment by  
606 a debris avalanche. The difference in the nature of the substrate from water-saturated,  
607 homogenous seafloor sediments below SLD2 and a denser and more heterogenous  
608 volcanoclastic substrate below SLD1, minimized the substrate incorporation and kinetic energy  
609 loss in SLD1. This led not only to a smaller total volume of SLD1 but also to a longer runout  
610 compared to the debris avalanche component of SLD2.

611

#### 612 5.4 Tsunami hazard

613 Landslides are the second most common trigger for tsunamis (Harbitz et al 2014) and have  
614 received increased attention with the 2018 Anak Krakatau flank collapse (Grilli et al., 2019).  
615 Numerical tsunami simulations of this event were conducted assuming a volume of initially  
616  $0.22 - 0.3 \text{ km}^3$  of volcanic material, which was inferred from pre- and post-collapse aerial and  
617 satellite imagery and produced results that were consistent with the observed wave  
618 characteristics and run-up heights (Grilli et al., 2019). However, numerical landslide tsunami



619 simulations rely heavily on the applied input parameters. In case of submarine landslides, the  
620 most important tsunami source parameters are the slide volume and its emplacement velocity  
621 (Løvholt et al., 2005), which are only poorly constrained for most historic events (with Ritter  
622 Island being a rare exception). Instead, volume estimations are often based on acoustic imaging  
623 data of flank collapse deposits, such as bathymetric and seismic data. Our results on SLD2 as  
624 well as those from Montserrat and Ritter (Karstens et al., 2019; Watt et al., 2012a) show that  
625 estimating the volume of the initial volcanic debris avalanche only from the surface area of a  
626 landslide deposit and the thickness of a stratigraphic unit can be misleading. Without high-  
627 resolution seismic data, SLD2 could be easily misinterpreted as one unit of chaotic reflections  
628 that resulted from a single-event debris avalanche. The actual volume of the debris avalanche  
629 component in SLD2 is less than half that of the complete stratigraphic unit, while the remainder  
630 consists of deformed or mobilized seafloor sediments. This underlines the necessity of high-  
631 resolution seismic data for accurate volume estimations and tsunami modelling constraints.

632 The second important constraint in tsunami modelling is the emplacement velocity, which is  
633 likely heavily influenced by interaction of the slide mass and the substrate causing a transfer of  
634 kinetic energy. A more rapid deceleration of the sliding mass (if occurring in water depths  
635 relevant for tsunami genesis) would reduce the magnitude of the resulting tsunami, while the  
636 effect of substrate incorporation (increasing the water column) has little impact compared to  
637 the initial volcanic flank component. Numerical tsunami simulations of the 1888 Ritter Island  
638 sector collapse suggest that tsunami generation was primarily controlled by the collapse of the  
639 volcano, i.e. the initial failure volume and acceleration, and that deeper seated deformation and  
640 seafloor sediment incorporation had no significant effect on the tsunami amplitude (Karstens et  
641 al., 2020). This is in agreement with tsunami potential calculations for landslide deposits off  
642 Montserrat, which have shown that tsunami amplitudes for submarine sediment failures with  
643 an associated low height drop are an order of magnitude smaller than flank collapse-related  
644 tsunami amplitudes of the same volume (Watt et al., 2012a). Hence, it is unlikely that the

645 seafloor sediment failure and deformation imaged in the middle and distal parts of SLD2  
646 affected the tsunami amplitude significantly, although they may result in longer wavelengths,  
647 as shown by a tsunami model for Deposit 2 off Montserrat (Watt et al., 2012a). Our analysis  
648 reveals once again that the complexity of volcanic sector collapse and debris avalanche  
649 emplacement in island settings, and highlights that tsunami hazard assessment for this  
650 comparably common process is still lacking reliable constraints for the most important source  
651 parameters.

652

## 653 6. Conclusions

654 The slope west of Sakar hosts two previously unknown landslide deposits. The younger deposit,  
655 SLD1, comprises volcanic debris avalanche material from Sakar, whereas the deeper SLD2 is  
656 a combination of a primary debris avalanche deposit and deformed and incorporated substrate.  
657 The toe domain of SLD2, which hosts folded and thrust-faulted sediments was shortened by at  
658 least 27 %. We suggest that the debris avalanche component of SLD2 partly eroded into and  
659 overran the substrate and triggered a progressive, lateral increase of the sediment pore pressure,  
660 resulting in a decrease of shear strength in the direction of the initial mass movement and  
661 mobilization and deformation of the pre-slide subsurface stratigraphy. We propose that the  
662 nature of the slide plane substrate is the most important control on sediment mobilization and  
663 secondary failures, and that this determined the different sizes and evolution of the two  
664 landslide deposits west of Sakar, which originated from the same source and were deposited on  
665 the same slope.

666 The main controlling parameters of landslide-generated tsunami amplitudes are the initial  
667 volume of the sliding mass that interacts with the ocean and its further acceleration. Estimating  
668 the initial volume of a flank or sector collapse by calculating the volume of the associated

669 landslide deposits involves a significant uncertainty. For SLD2 there is evidence that less than  
670 half of the landslide deposit's volume can be assigned to the initial debris avalanche.

671

## 672 7. Acknowledgements

673 We thank the master and the crew of the RV SONNE for their support during research cruise  
674 SO252. We also thank Dr. Ingo Klaucke and Dr. Christoph Böttner for the onboard-processing  
675 of the bathymetry data. We acknowledge Kei Ogata, Fabiano Gamberi and Derek Sawyer for  
676 improving the quality of the manuscript with their reviews. We would like to thank the GEBCO  
677 initiative for providing access to global digital elevation data and Schlumberger and IHS for  
678 granting educational software licenses for the interpretation of the seismic data. The German  
679 Ministry of Science and Education (BMBF) funded this study through the “Ritter Island  
680 project” grant [03G0252A].

681

## 682 8. Data Availability

683 The datasets analyzed in this study will be publicly available at the PANGAEA data  
684 repository (multibeam echosounder data: <https://doi.org/10.1594/PANGAEA.929026>, seismic  
685 data: <https://doi.org/10.1594/PANGAEA.929022>), once this article is published.

686

## 687 9. References

- 688 Alves, T.M., Lourenço, S.D.N., 2010. Geomorphologic features related to gravitational  
689 collapse: Submarine landsliding to lateral spreading on a Late Miocene-Quaternary slope  
690 (SE Crete, eastern Mediterranean). *Geomorphology* 123, 13–33.  
691 <https://doi.org/10.1016/j.geomorph.2010.04.030>
- 692 Baldwin, S.L., Fitzgerald, P.G., Webb, L.E., 2012. Tectonics of the New Guinea Region.  
693 *Annu. Rev. Earth Planet. Sci.* 40, 495–520. [https://doi.org/10.1146/annurev-earth-](https://doi.org/10.1146/annurev-earth-040809-152540)  
694 [040809-152540](https://doi.org/10.1146/annurev-earth-040809-152540)

695 Berndt, C., Klauke, I., Kühn, M., 2021a. Multibeam bathymetry gridded data from SONNE  
696 cruise SO252. <https://doi.org/https://doi.org/10.1594/PANGAEA.929026>

697 Berndt, C., Kühn, M., Karstens, J., 2021b. 2D multi-channel seismic data from SONNE cruise  
698 SO252 offshore Ritter Island, 2016, Bismarck Sea, Papua New Guinea.  
699 <https://doi.org/10.1594/PANGAEA.929022>

700 Berndt, C., Muff, S., Klauke, I., Watt, S., Böttner, C., Schramm, B., Völsch, A.-M.,  
701 Bennecke, S., Elger, J., Chi, W.-C., Van Haren, J., Micallef, A., Roth, T., 2016. RV  
702 SONNE 252 Cruise Report / Fahrtbericht Tsunami potential of volcanic flank collapses  
703 Table of content. [https://doi.org/http://dx.doi.org/10.3289/CR\\_SO252](https://doi.org/http://dx.doi.org/10.3289/CR_SO252)

704 Bjerrum, L., 1955. Stability of natural slopes in quick clay. *Géotechnique* 5, 101–119.  
705 <https://doi.org/https://doi.org/10.1680/geot.1955.5.1.101>

706 Crutchley, G.J., Karstens, J., Berndt, C., Talling, P.J., Watt, S.F.L., Vardy, M.E., Hühnerbach,  
707 V., Urlaub, M., Sarkar, S., Klaeschen, D., Paulatto, M., Le Friant, A., Lebas, E., Maeno,  
708 F., 2013. Insights into the emplacement dynamics of volcanic landslides from high-  
709 resolution 3D seismic data acquired offshore Montserrat, Lesser Antilles. *Mar. Geol.*  
710 335, 1–15. <https://doi.org/10.1016/j.margeo.2012.10.004>

711 Day, S., Llanes, P., Silver, E., Hoffmann, G., Ward, S., Driscoll, N., 2015. Submarine  
712 landslide deposits of the historical lateral collapse of Ritter Island, Papua New Guinea.  
713 *Mar. Pet. Geol.* 67, 419–438. <https://doi.org/10.1016/j.marpetgeo.2015.05.017>

714 Day, S.J., Heleno Da Silva, S.I.N., Fonseca, J.F.B.D., 1999. A past giant lateral collapse and  
715 present-day flank instability of Fogo, Cape Verde Islands. *J. Volcanol. Geotherm. Res.*  
716 94, 191–218. [https://doi.org/10.1016/S0377-0273\(99\)00103-1](https://doi.org/10.1016/S0377-0273(99)00103-1)

717 De Blasio, F.V., Elverhøi, A., Issler, D., Harbitz, C.B., Bryn, P., Lien, R., 2005. On the  
718 dynamics of subaqueous clay rich gravity mass flows - The giant Storegga slide,  
719 Norway. *Mar. Pet. Geol.* 22, 179–186. <https://doi.org/10.1016/j.marpetgeo.2004.10.014>

720 Deplus, C., Le Friant, A., Boudon, G., Komorowski, J.C., Villemant, B., Harford, C.,

721 Ségoufin, J., Cheminée, J.L., 2001. Submarine evidence for large-scale debris avalanches  
722 in the Lesser Antilles Arc. *Earth Planet. Sci. Lett.* 192, 145–157.  
723 [https://doi.org/10.1016/S0012-821X\(01\)00444-7](https://doi.org/10.1016/S0012-821X(01)00444-7)

724 Frey-Martínez, J., Cartwright, J., James, D., 2006. Frontally confined versus frontally  
725 emergent submarine landslides: A 3D seismic characterisation. *Mar. Pet. Geol.* 23, 585–  
726 604. <https://doi.org/10.1016/j.marpetgeo.2006.04.002>

727 Gee, M.J.R., Uy, H.S., Warren, J., Morley, C.K., Lambiase, J.J., 2007. The Brunei slide: A  
728 giant submarine landslide on the North West Borneo Margin revealed by 3D seismic  
729 data. *Mar. Geol.* 246, 9–23. <https://doi.org/10.1016/j.margeo.2007.07.009>

730 Glicken, H., 1996. Rockslide-debris avalanche of may 18, 1980, Mount St. Helens volcano,  
731 Washington. Open-file Rep. 96-677 1–5.

732 Gouhier, M., Paris, R., 2019. SO<sub>2</sub> and tephra emissions during the December 22, 2018 Anak  
733 Krakatau flank-collapse eruption. *Volcanica* 2, 91–103.  
734 <https://doi.org/10.30909/vol.02.02.91103>

735 Grilli, S.T., Tappin, D.R., Carey, S., Watt, S.F.L., Ward, S.N., Grilli, A.R., Engwell, S.L.,  
736 Zhang, C., Kirby, J.T., Schambach, L., Muin, M., 2019. Modelling of the tsunami from  
737 the December 22, 2018 lateral collapse of Anak Krakatau volcano in the Sunda Straits,  
738 Indonesia. *Sci. Rep.* 9, 1–13. <https://doi.org/10.1038/s41598-019-48327-6>

739 Holm, R.J., Richards, S.W., 2013. A re-evaluation of arc-continent collision and along-arc  
740 variation in the Bismarck Sea region, Papua New Guinea. *Aust. J. Earth Sci.* 60, 605–  
741 619. <https://doi.org/10.1080/08120099.2013.824505>

742 Honza, E., Miyazaki, T., Lock, J., 1989. Subduction erosion and accretion in the Solomon Sea  
743 region. *Tectonophysics* 160, 49–62. [https://doi.org/10.1016/0040-1951\(89\)90383-1](https://doi.org/10.1016/0040-1951(89)90383-1)

744 Hornbach, M.J., Manga, M., Genecov, M., Valdez, R., Miller, P., Saffer, D., Adelstein, E.,  
745 Lafuerza, S., Adachi, T., Breitkreuz, C., Jutzeler, M., LeFriant, A., Ishizuka, O., Morgan,  
746 S., Slagle, A., Talling, P.J., Fraass, A., Watt, S.F.L., Stroncik, N.A., Aljehdali, M.,

747 Boudon, G., Fujinawa, A., Hatfield, R., Kataoka, K., Maeno, F., Martinez-Colon, M.,  
748 McCanta, M., Palmer, M., Stinton, A., Subramanyam, K.S. V., Tamura, Y., Villemant,  
749 B., Wall-Palmer, D., Wang, and F., 2015. Permeability and pressure measurements in  
750 Lesser Antilles submarine slides: Evidence for pressure-driven slow-slip failure. *J.*  
751 *Geophys. Res. Solid Earth* 120, 7986–8011. <https://doi.org/10.1002/2015JB012061>

752 Johnson, R., Kitts, S., Indies, W., Roobol, M.J., I, A.L.S., Wright, J. V, 1987. Large-scale  
753 volcanic cone collapse: the 1888 slope failure of Ritter volcano, and other examples from  
754 Papua New Guinea. *Bull. Volcanol.* 49, 669–679.

755 Johnson, R.W., 1977. Distribution and major-element chemistry of late Cainozoic vol-  
756 canoes at the southern margin of the Bismarck Sea, PNG. *Aust. Bur. Miner. Resour. Geol.*  
757 *Geophys. Rep.*188. 162 pp.

758 Karstens, J., Berndt, C., Urlaub, M., Watt, S.F.L., Micallef, A., Ray, M., Klauke, I., Muff, S.,  
759 Klaeschen, D., Kühn, M., Roth, T., Böttner, C., Schramm, B., Elger, J., Brune, S., 2019.  
760 From gradual spreading to catastrophic collapse – Reconstruction of the 1888 Ritter  
761 Island volcanic sector collapse from high-resolution 3D seismic data. *Earth Planet. Sci.*  
762 *Lett.* 517, 1–13. <https://doi.org/10.1016/j.epsl.2019.04.009>

763 Karstens, J., Crutchley, G.J., Berndt, C., Talling, P.J., Watt, S.F.L., Hühnerbach, V., Friant,  
764 A. Le, Lebas, E., Trofimovs, J., 2013. Emplacement of pyroclastic deposits offshore  
765 Montserrat: Insights from 3D seismic data. *J. Volcanol. Geotherm. Res.* 257, 1–11.  
766 <https://doi.org/10.1016/j.jvolgeores.2013.03.004>

767 Karstens, J., Kelfoun, K., Watt, S.F.L., Berndt, C., 2020. Combining 3D seismics, eyewitness  
768 accounts and numerical simulations to reconstruct the 1888 Ritter Island sector collapse  
769 and tsunami. *Int. J. Earth Sci.* <https://doi.org/10.1007/s00531-020-01854-4>

770 Le Bas, T.P., Masson, D.G., Holtom, R.T., Grevemeyer, I., 2007. Slope failures of the flanks  
771 of the southern Cape Verde Islands. *Submar. Mass Movements Their Consequences*, 3rd  
772 *Int. Symp.* 337–345. [https://doi.org/10.1007/978-1-4020-6512-5\\_35](https://doi.org/10.1007/978-1-4020-6512-5_35)

773 Le Friant, A., 2015. Geochemistry, Geophysics, Geosystems. *Geochemistry Geophys.*  
774 *Geosystems* 18, 1541–1576. <https://doi.org/10.1002/2014GC005684>.Key

775 Le Friant, A., Boudon, G., Deplus, C., Villemant, B., 2003. Large-scale flank collapse events  
776 during the activity of Montagne Pelée, Martinique, Lesser Antilles. *J. Geophys. Res.*  
777 *Solid Earth* 108, 1–15. <https://doi.org/10.1029/2001jb001624>

778 Lenz, B.L., Sawyer, D.E., Phrampus, B., Davenport, K., Long, A., 2019. Seismic imaging of  
779 seafloor deformation induced by impact from large submarine landslide blocks, offshore  
780 oregon. *Geosci.* 9. <https://doi.org/10.3390/geosciences9010010>

781 Løvholt, F., Harbitz, C.B., Haugen, K.B., 2005. A parametric study of tsunamis generated by  
782 submarine slides in the Ormen Lange/Storegga area off western Norway. *Mar. Pet. Geol.*  
783 22, 219–231. <https://doi.org/10.1016/j.marpetgeo.2004.10.017>

784 Løvholt, F., Pedersen, G., Harbitz, C.B., Glimsdal, S., Kim, J., 2015. On the characteristics of  
785 landslide tsunamis. *Philos. Trans. R. Soc. A Math. Phys. Eng. Sci.* 373.  
786 <https://doi.org/10.1098/rsta.2014.0376>

787 Mangeney, A., Roche, O., Hungr, O., Mangold, N., Faccanoni, G., Lucas, A., 2010. Erosion  
788 and mobility in granular collapse over sloping beds. *J. Geophys. Res. Earth Surf.* 115, 1–  
789 21. <https://doi.org/10.1029/2009JF001462>

790 Masson, D.G., Le Bas, T.P., Grevemeyer, I., Weinrebe, W., 2008. Flank collapse and large-  
791 scale landsliding in the Cape Verde Islands, off West Africa. *Geochemistry, Geophys.*  
792 *Geosystems* 9, 1–16. <https://doi.org/10.1029/2008GC001983>

793 Masson, D.G., Watts, A.B., Gee, M.J.R., Urgeles, R., Mitchell, N.C., Le Bas, T.P., Canals,  
794 M., 2002. Slope failures on the flanks of the western Canary Islands. *Earth-Science Rev.*  
795 57, 1–35. [https://doi.org/10.1016/S0012-8252\(01\)00069-1](https://doi.org/10.1016/S0012-8252(01)00069-1)

796 Mohrig, D., Whipple, K.X., Hondzo, M., Ellis, C., Parker, G., 1998. Hydroplaning of  
797 subaqueous debris flows. *Bull. Geol. Soc. Am.* 110, 387–394.  
798 [https://doi.org/10.1130/0016-7606\(1998\)110<0387:HOSDF>2.3.CO;2](https://doi.org/10.1130/0016-7606(1998)110<0387:HOSDF>2.3.CO;2)

799 Morita, S., Nakajima, T., Hanamura, Y., 2011. Submarine slump sediments and related  
800 dewatering structures: Observations of 3D seismic data obtained for the continental slope  
801 off Shimokita Peninsula, NE Japan. *J. Geol. Soc. Japan* 117, 95–98.  
802 <https://doi.org/10.5575/geosoc.117.95>

803 Mulder, T., Cochonat, P., 1996. Classification of offshore mass movements. *J. Sediment. Res.*  
804 66, 43–57.

805 Ogata, K., Festa, A., Pini, G.A., Pogačnik, Lucente, C.C., 2019. Substrate deformation and  
806 incorporation in sedimentary mélanges (olistostromes): Examples from the northern  
807 Apennines (Italy) and northwestern Dinarides (Slovenia). *Gondwana Res.* 74, 101–125.  
808 <https://doi.org/10.1016/j.gr.2019.03.001>

809 Ogata, K., Mountjoy, J.J., Pini, G.A., Festa, A., Tinterri, R., 2014a. Shear zone liquefaction in  
810 mass transport deposit emplacement: A multi-scale integration of seismic reflection and  
811 outcrop data. *Mar. Geol.* 356, 50–64. <https://doi.org/10.1016/j.margeo.2014.05.001>

812 Ogata, K., Mutti, E., Pini, G.A., Tinterri, R., 2012. Mass transport-related stratal disruption  
813 within sedimentary mélanges: Examples from the northern Apennines (Italy) and south-  
814 central Pyrenees (Spain). *Tectonophysics* 568–569, 185–199.  
815 <https://doi.org/10.1016/j.tecto.2011.08.021>

816 Ogata, K., Pogačnik, Z., Pini, G.A., Tunis, G., Festa, A., Camerlenghi, A., Rebesco, M.,  
817 2014b. The carbonate mass transport deposits of the Paleogene Friuli Basin  
818 (Italy/Slovenia): Internal anatomy and inferred genetic processes. *Mar. Geol.* 356, 88–  
819 110. <https://doi.org/10.1016/j.margeo.2014.06.014>

820 Pope, E.L., Jutzeler, M., Cartigny, M.J.B., Shreeve, J., Talling, P.J., Wright, I.C.,  
821 Wysoczanski, R.J., 2018. Origin of spectacular fields of submarine sediment waves  
822 around volcanic islands. *Earth Planet. Sci. Lett.* 493, 12–24.  
823 <https://doi.org/10.1016/j.epsl.2018.04.020>

824 Quinn, P.E., Diederichs, M.S., Rowe, R.K., Hutchinson, D.J., 2012. Development of



825 progressive failure in sensitive clay slopes. *Can. Geotech. J.* 49, 782–795.  
826 <https://doi.org/10.1139/T2012-034>

827 Siebert, L., 1984. Large volcanic debris avalanches: Characteristics of source areas, deposits,  
828 and associated eruptions. *J. Volcanol. Geotherm. Res.* 22, 163–197.  
829 [https://doi.org/10.1016/0377-0273\(84\)90002-7](https://doi.org/10.1016/0377-0273(84)90002-7)

830 Siebert, L., Roverato, M., 2021. A Historical Perspective on Lateral Collapse and Volcanic  
831 Debris Avalanches, in: Roverato, M., Dufresne, A., Procter, J. (Eds.), *Volcanic Debris*  
832 *Avalanches: From Collapse to Hazard*. Springer International Publishing, Cham, pp. 11–  
833 50. [https://doi.org/10.1007/978-3-030-57411-6\\_2](https://doi.org/10.1007/978-3-030-57411-6_2)

834 Silver, E., Day, S., Ward, S., Hoffmann, G., Llanes, P., Driscoll, N., Appelgate, B., Saunders,  
835 S., 2009. Volcano collapse and tsunami generation in the Bismarck Volcanic Arc, Papua  
836 New Guinea. *J. Volcanol. Geotherm. Res.* 186, 210–222.  
837 <https://doi.org/10.1016/j.jvolgeores.2009.06.013>

838 Sobiesiak, M.S., Kneller, B., Alsop, G.I., Milana, J.P., 2018. Styles of basal interaction  
839 beneath mass transport deposits. *Mar. Pet. Geol.* 98, 629–639.  
840 <https://doi.org/10.1016/j.marpetgeo.2018.08.028>

841 Taylor, B., 1979. Bismarck Sea: Evolution of a back-arc basin. *Geology* 7, 171–174.  
842 [https://doi.org/10.1130/0091-7613\(1979\)7<171:BSEOAB>2.0.CO;2](https://doi.org/10.1130/0091-7613(1979)7<171:BSEOAB>2.0.CO;2)

843 Urlaub, M., Petersen, F., Gross, F., Bonforte, A., Puglisi, G., Guglielmino, F., Krastel, S.,  
844 Lange, D., Kopp, H., 2018. Gravitational collapse of Mount Etna’s southeastern flank.  
845 *Sci. Adv.* 4, 1–8. <https://doi.org/10.1126/sciadv.aat9700>

846 Van Der Merwe, W.C., Hodgson, D.M., Flint, S.S., 2011. Origin and terminal architecture of  
847 a submarine slide: A case study from the Permian Vischkuil Formation, Karoo Basin,  
848 South Africa. *Sedimentology* 58, 2012–2038. [https://doi.org/10.1111/j.1365-](https://doi.org/10.1111/j.1365-3091.2011.01249.x)  
849 [3091.2011.01249.x](https://doi.org/10.1111/j.1365-3091.2011.01249.x)

850 Walter, T.R., Haghshenas Haghghi, M., Schneider, F.M., Coppola, D., Motagh, M., Saul, J.,

851 Babeyko, A., Dahm, T., Troll, V.R., Tilmann, F., Heimann, S., Valade, S., Triyono, R.,  
852 Khomarudin, R., Kartadinata, N., Laiolo, M., Massimetti, F., Gaebler, P., 2019. Complex  
853 hazard cascade culminating in the Anak Krakatau sector collapse. *Nat. Commun.* 10.  
854 <https://doi.org/10.1038/s41467-019-12284-5>

855 Ward, S.N., Day, S., 2003. Ritter Island Volcano - Lateral collapse and the tsunami of 1888.  
856 *Geophys. J. Int.* 154, 891–902. <https://doi.org/10.1046/j.1365-246X.2003.02016.x>

857 Watt, S.F.L., Karstens, J., Berndt, C., 2021. Volcanic-Island Lateral Collapses and Their  
858 Submarine Deposits, *Advances in Volcanology*. Springer International Publishing.  
859 [https://doi.org/10.1007/978-3-030-57411-6\\_10](https://doi.org/10.1007/978-3-030-57411-6_10)

860 Watt, S.F.L., Karstens, J., Micallef, A., Berndt, C., Urlaub, M., Ray, M., Desai, A.,  
861 Sammartini, M., Klauke, I., Böttner, C., Day, S., Downes, H., Kühn, M., Elger, J., 2019.  
862 From catastrophic collapse to multi-phase deposition: Flow transformation, seafloor  
863 interaction and triggered eruption following a volcanic-island landslide. *Earth Planet.*  
864 *Sci. Lett.* 517, 135–147. <https://doi.org/10.1016/j.epsl.2019.04.024>

865 Watt, S.F.L., Talling, P.J., Vardy, M.E., Heller, V., Hühnerbach, V., Urlaub, M., Sarkar, S.,  
866 Masson, D.G., Henstock, T.J., Minshull, T.A., Paulatto, M., Le Friant, A., Lebas, E.,  
867 Berndt, C., Crutchley, G.J., Karstens, J., Stinton, A.J., Maeno, F., 2012a. Combinations  
868 of volcanic-flank and seafloor-sediment failure offshore Montserrat, and their  
869 implications for tsunami generation. *Earth Planet. Sci. Lett.* 319–320, 228–240.  
870 <https://doi.org/10.1016/j.epsl.2011.11.032>

871 Watt, S.F.L., Talling, P.J., Vardy, M.E., Masson, D.G., Henstock, T.J., Hühnerbach, V.,  
872 Minshull, T.A., Urlaub, M., Lebas, E., Le Friant, A., Berndt, C., Crutchley, G.J.,  
873 Karstens, J., 2012b. Widespread and progressive seafloor-sediment failure following  
874 volcanic debris avalanche emplacement: Landslide dynamics and timing offshore  
875 Montserrat, Lesser Antilles. *Mar. Geol.* 323–325, 69–94.  
876 <https://doi.org/10.1016/j.margeo.2012.08.002>

877 Weiß, B.J., Hübscher, C., Wolf, D., Lüdmann, T., 2015. Submarine explosive volcanism in  
878 the southeastern Terceira Rift/São Miguel region (Azores). *J. Volcanol. Geotherm. Res.*  
879 303, 79–91. <https://doi.org/10.1016/j.jvolgeores.2015.07.028>

880 Woodhead, J., Hergt, J., Sandiford, M., Johnson, W., 2010. The big crunch: Physical and  
881 chemical expressions of arc/continent collision in the Western Bismarck arc. *J. Volcanol.*  
882 *Geotherm. Res.* 190, 11–24. <https://doi.org/10.1016/j.jvolgeores.2009.03.003>

883 Yoshida, H., Sugai, T., Ohmori, H., 2012. Geomorphology Size – distance relationships for  
884 hummocks on volcanic rockslide-debris avalanche deposits in Japan. *Geomorphology*  
885 136, 76–87. <https://doi.org/10.1016/j.geomorph.2011.04.044>

886

147° 40' E

WGS84

147° 50' E

148° 00' E

148° 10' E

4° 50' S

5° 00' S

5° 10' S

5° 20' S

5° 30' S

5° 40' S

transition of internally chaotic sub-facies  
to deformed sediment sub-facies within SLD2

valley- or channel-like  
morphology

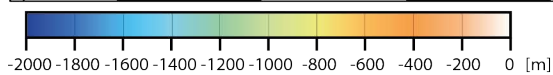
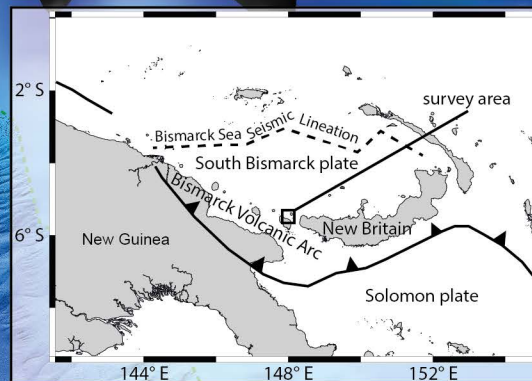
valley- or channel-like  
morphology

Sakar

Ritter

Umboi

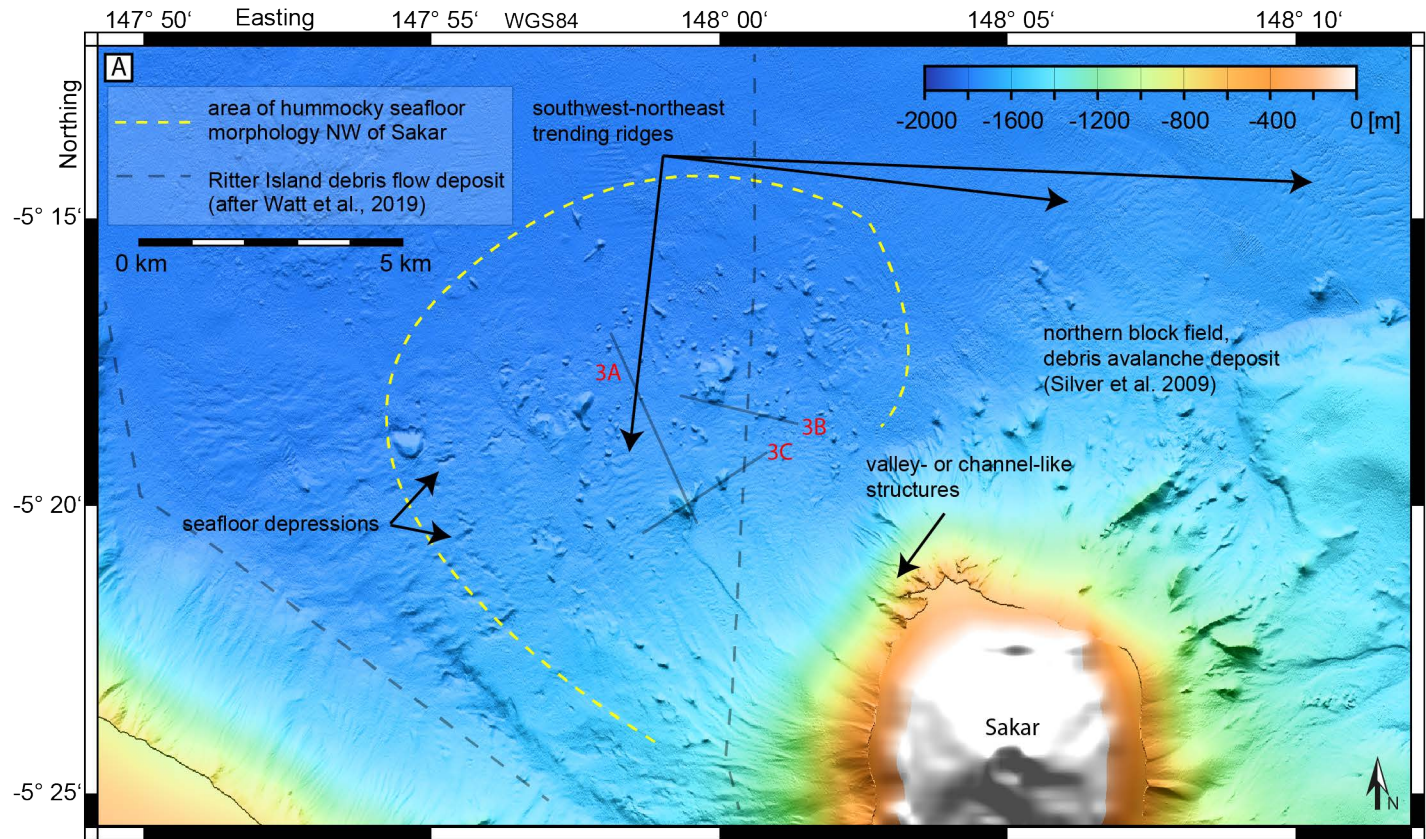
- extent SLD1
- extent SLD2
- SO252 2D MCS Profiles
- - - transition high-res.  
Bathymetry / GEBCO

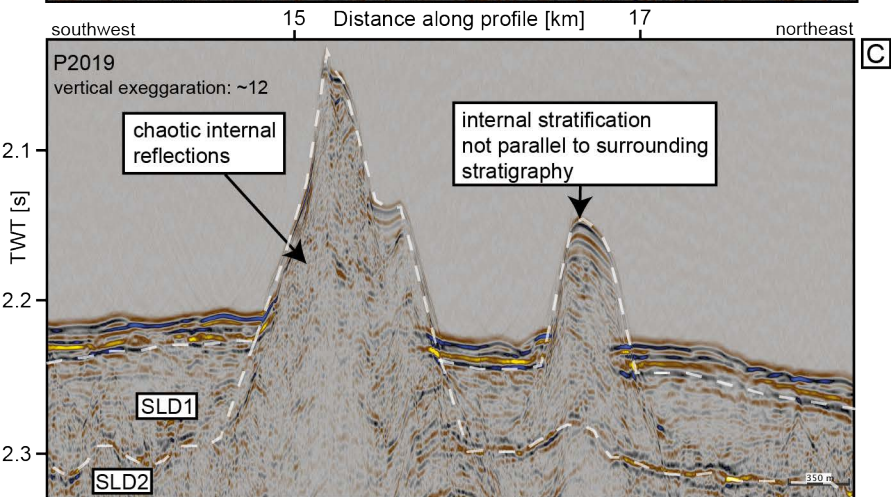
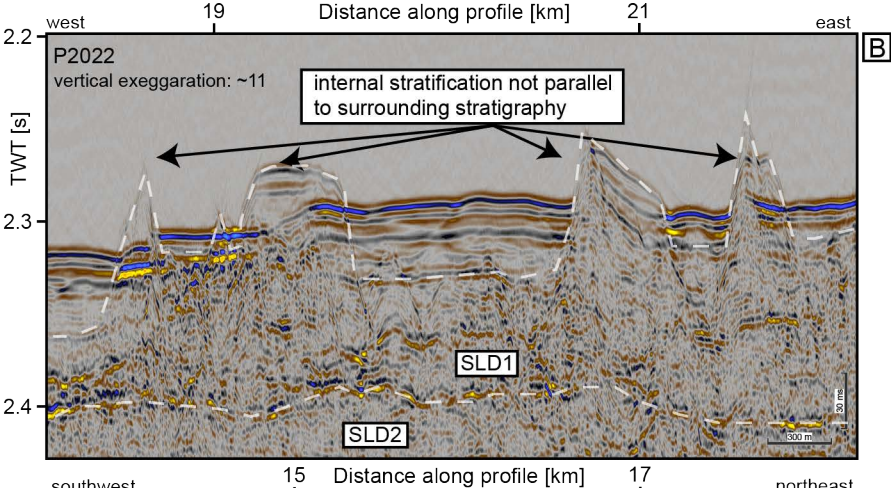
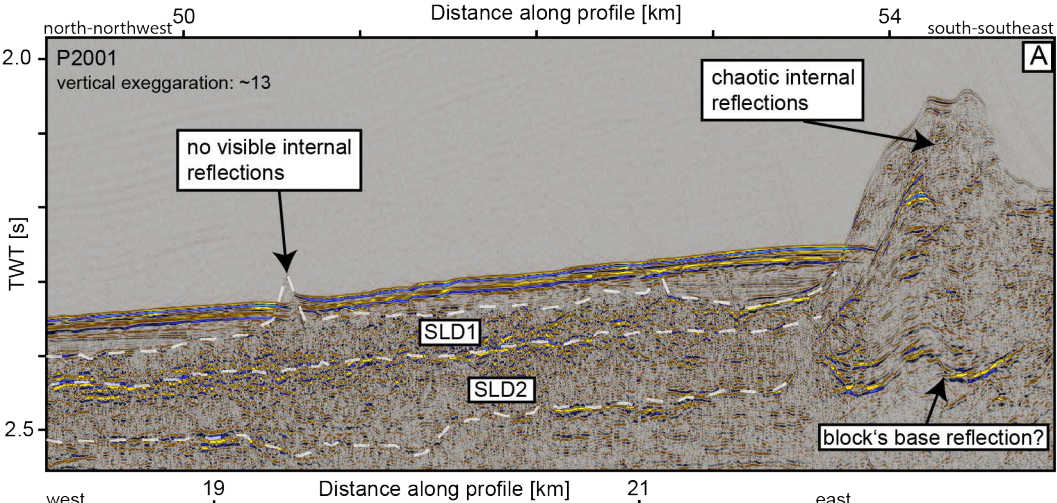


0 5 10 15 20 25 km

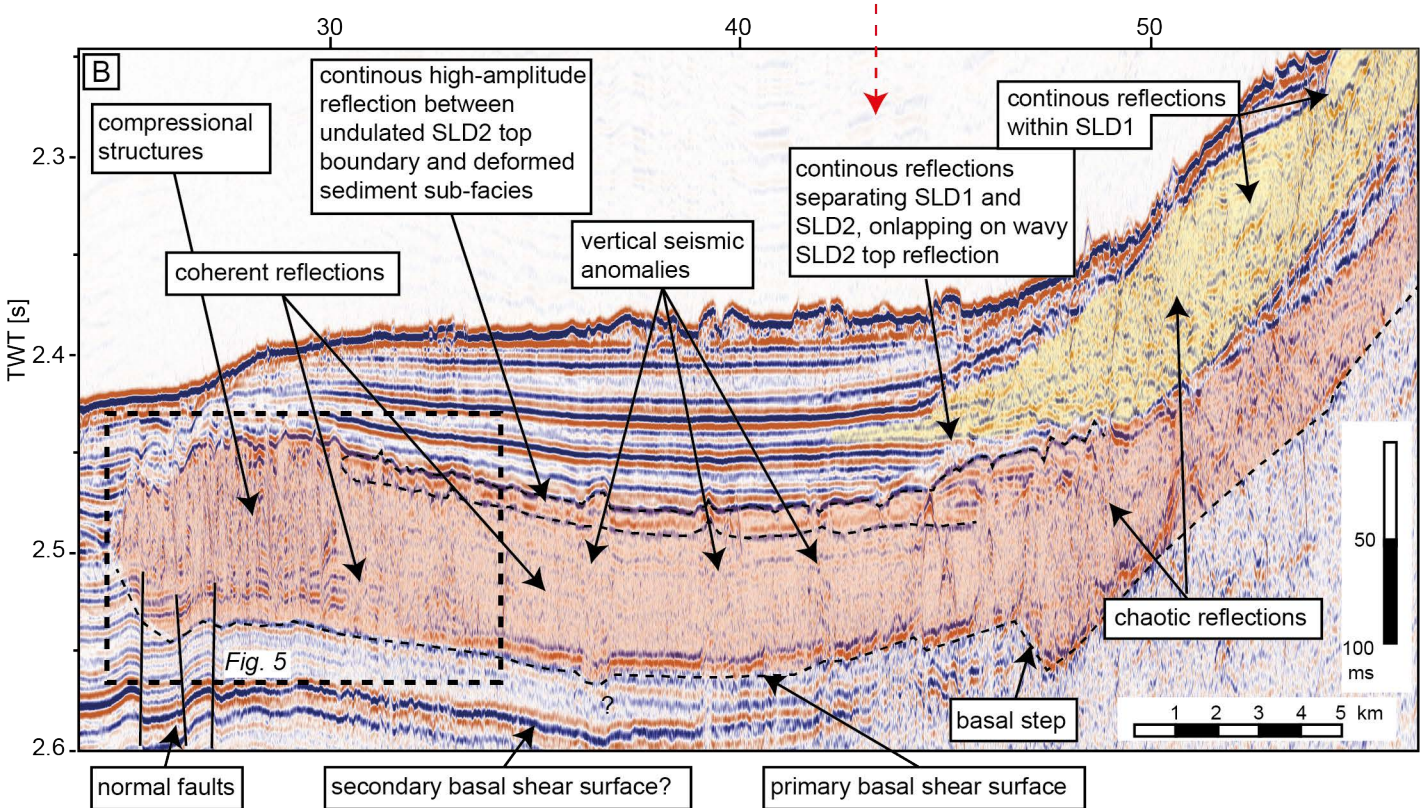
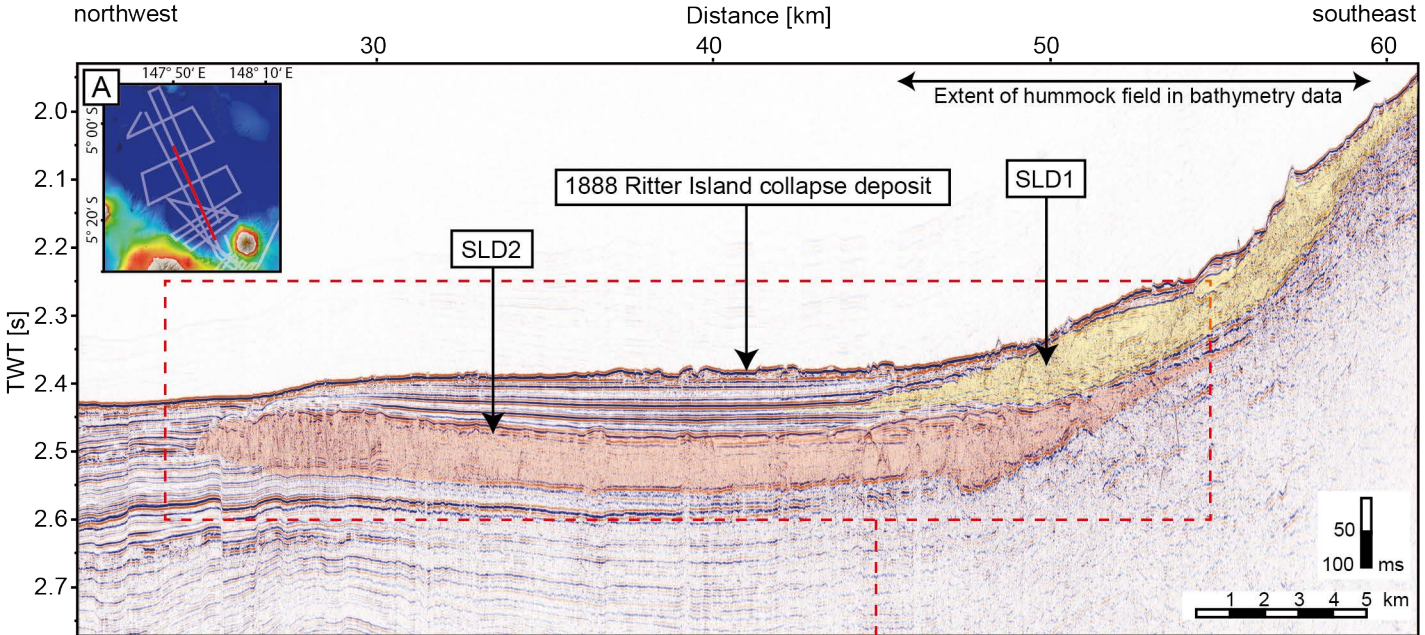












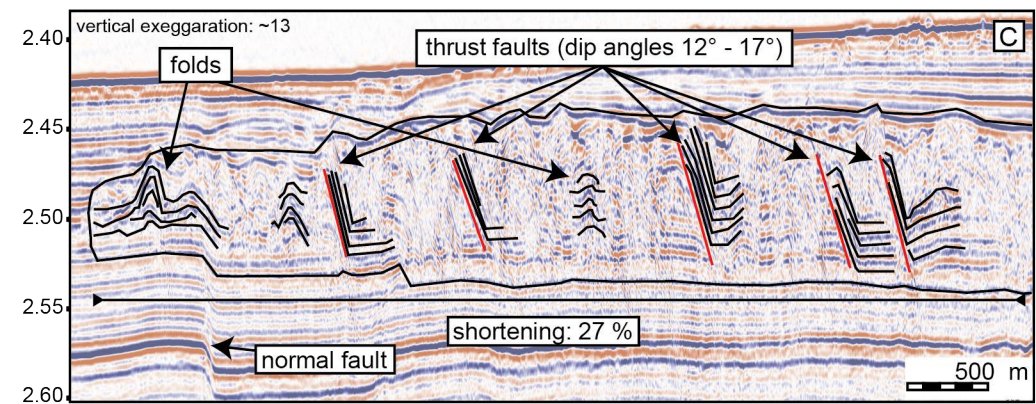
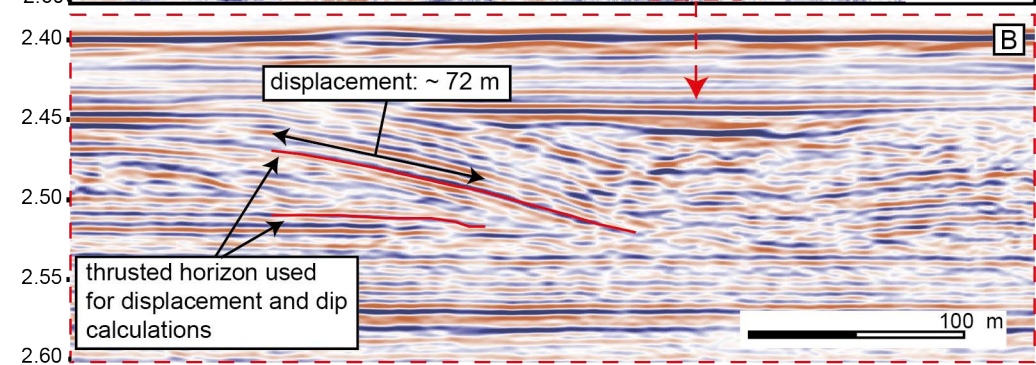
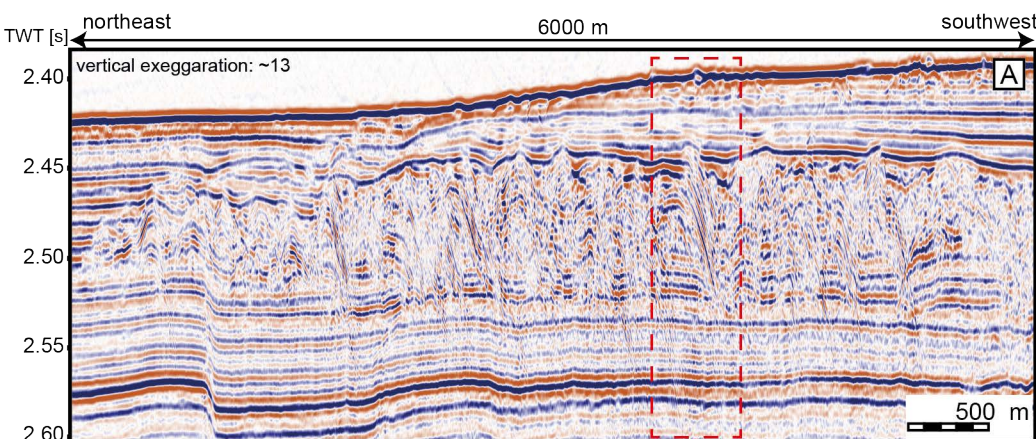
SLD2 structural configuration:

Distal:  
Compression  
(thrust faults, folds;  
deformed sediment  
sub-facies)

Middle:  
Parallel structure of reflections preserved,  
but transparent (deformed sediment  
sub-facies)

Proximal:  
Chaotic, incoherent reflections,  
transparent (internally chaotic sub-facies)







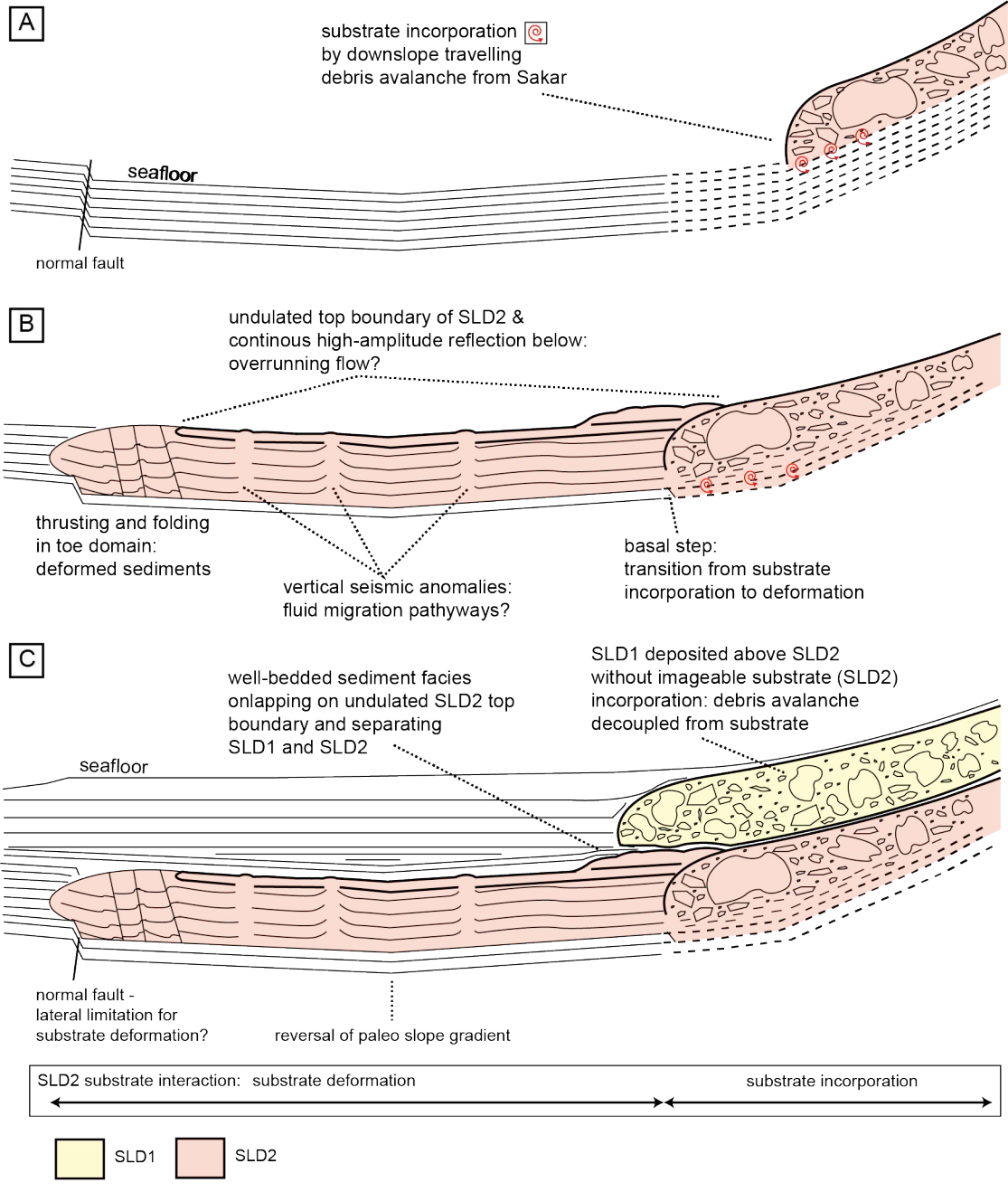


Figure 1: Map of the study region, showing the extents of SLD1 and SLD2 (dashed line indicates the limits of clear deposit imaging). The solid black lines mark acquired 2D multichannel seismic profiles (Karstens et al., 2019; Watt et al., 2019). Background: High-resolution bathymetry acquired during SO252 merged with low-resolution GEBCO grid (transition at dotted green line). Right corner: Overview map showing the general tectonic setting of the area.

Figure 2: A: Bathymetry of the hummock field northwest of Sakar. The dashed yellow line marks the extent of the hummock field, broadly coinciding with the margin of SLD1 in seismic reflection profiles. The dashed grey lines mark the margins of the 1888 Ritter Island collapse deposit, after Watt et al. (2019). Grey lines mark the locations of the seismic sections shown in Fig. 3A, 3B and 3C.

Figure 3: Selected seismic-reflection profiles through SLD1 and SLD2 (locations on Fig. 2). A: Profile across a ~900 m wide hummock with chaotic internal stratification (right) and a hummock with no visible internal reflections (left). The large hummock appears to be rooted within SLD2. B: Profile showing four hummocks apparently rooted within SLD1, which are either seismically transparent (low amplitude) or have stratigraphically chaotic internal structures or stratification that is not parallel to the surrounding stratigraphy. C: Profile showing the 900-m-wide hummock from A in an orthogonal direction and another, smaller hummock with stratification not parallel to the surroundings. In all panels, dashed lines indicate the top and bottom boundaries of SLD1 and SLD2.

Figure 4: Northwest-southeast oriented seismic section showing SLD1 and SLD2 with annotated interpretations. A: Extent of SLD1, SLD2 and the 1888 Ritter Island collapse deposit (see inset map). B: Detail of the internal architecture of SLD1 and SLD2.

Figure 5: A: Profile through the distal section of SLD2, revealing compressional structures including thrust faults and folds, over ~5 km. B: Detail of a thrust fault without vertical exaggeration. C: Interpreted version of Panel A, showing horizons used to constrain the minimum magnitude of shortening.

Figure 6: Model for the emplacement of SLD1 and SLD2. A: A blocky debris avalanche associated with SLD2 flowing downslope, starting to incorporate and incise into the substrate. Different specific incorporation mechanisms are discussed in the text. B: The situation after the emplacement of SLD2, showing substrate incorporation (right) and frontal, downslope deformation, driven by impact and augmented by an overrunning flow, derived from the initial debris avalanche. The distal deformation limit is associated with a pre-existing fault, disrupting the stratigraphy, and a reversal in the paleo-basin slope gradient. C: The situation before the Ritter Island 1888 landslide deposit, showing the blocky debris avalanche of SLD1, emplaced above SLD2 without incorporating the substrate (SLD2 and the relatively thin intervening sediment package), indicating a decoupling of the slide mass from the substrate. Both landslides have been subsequently buried by younger basin infill.